

Achieving high resolution with an all-digital associated particle imaging system for the 3D determination of isotopic distributions

Mauricio Ayllon Unzueta,^{a)} Bernhard Ludewigt, Tanay Tak, and Arun Persaud^{b)}

Acceleration Technology & Applied Physics

Lawrence Berkeley National Laboratory

1 Cyclotron Road, CA 94720, USA

(Dated: 6 June 2022)

Associated particle imaging (API) is a non-destructive nuclear technique for the 3D determination of isotopic distributions. By detecting the alpha particle associated with the emitted neutron in the deuterium-tritium fusion reaction with a position and time resolving detector, the direction of the 14.1 MeV neutron and its time of emission can be determined. Employing this method, isotope characteristic gamma rays emitted in inelastic neutron scattering events can be correlated with the neutron interaction location. An API system consisting of a sealed-type neutron generator, gamma detectors, and a position-sensitive alpha detector was designed, constructed, and characterized. The system was tested with common soil elements and shown to be sensitive to ^{12}C , ^{16}O , ^{28}Si , ^{27}Al , and ^{56}Fe . We present a description of the system with simulations and experimental results indicating a lateral (X-Y) resolution of 2 to 4 cm and a depth (Z) resolution of 6.2 cm for measurements performed with a lanthanum bromide gamma-ray detector. Additionally, we present single-element gamma response measurements for the elements mentioned above together with a comparison to Monte Carlo simulations (MCNP6).

I. INTRODUCTION

Non-destructive carbon-in-soil measurement methods are important for understanding and quantifying soil-based carbon sequestration techniques on a large scale since soil is the largest storage pool of terrestrial carbon¹. Monitoring carbon in soil also supports improvements in soil health and crop yield². The standard procedure to measure carbon concentration in soils today consists of taking core (point) samples and analyzing them in a chemistry lab using loss on ignition (LOI) techniques³. This destructive procedure takes from a few days to weeks before results are obtained, and results from a few sampling points are then often used to extrapolate the carbon distribution for an entire field or larger areas. As part of an ARPA-e⁴ funded effort to develop better sensors for soil and imaging of roots, we are developing an API instrument for quantifying carbon distributions in soil. This instrument, when fully developed into a commercial system, is expected to be able to non-destructively analyze soil volumes ($50 \times 50 \times 30 \text{ cm}^3$) *in-situ* within minutes depending on carbon concentration, allowing better estimates on a field scale. Additionally, its capabilities allow for centimeter resolution in all three dimensions in order to account for carbon heterogeneity. Non-API neutron based methods for soil characterization have been reported before^{5,6}, including instruments that are using time-tagged neutron signals⁷ and pulsed neutron generators⁸.

The API system consists of a sealed-type neutron generator, an alpha particle detector, and two gamma-ray detectors, i.e. a lanthanum bromide (LaBr_3) and a sodium iodide (NaI) scintillation detectors. These components are arranged as schematically shown in Figure 1.

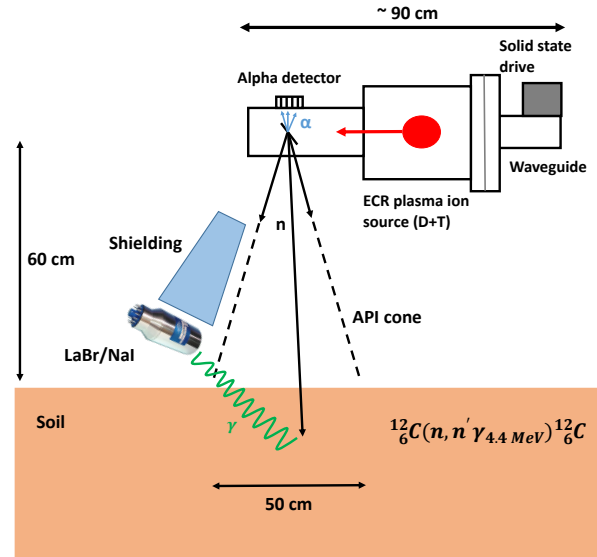
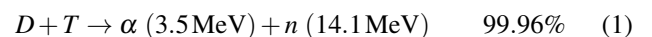


FIG. 1. Schematic illustration of the API technique. 14.1 MeV neutrons are produced in a sealed-type neutron generator equipped with a position-sensitive alpha detector. Neutron-induced inelastic gamma rays (e.g. from ^{12}C) are generated in the sample (soil) and detected with a LaBr_3 or NaI detector.

The neutron generator works by accelerating a charged particle beam consisting of deuterium (D) and tritium (T) ions onto a titanium target where they accumulate and undergo DT fusion reactions within a small surface area of approximately 2 mm in diameter. The nuclear reaction shown in Equation 1 results in a two-particle decay, and hence the neutron and the alpha particle are emitted back-to-back in the center-of-mass reference frame with fixed energies.



^{a)}Electronic mail: mayllon@berkeley.edu; Also at Nuclear Engineering Department, University of California, Berkeley.; Now at Solar system exploration division, NASA Goddard Space Flight Center, Greenbelt, Maryland.

^{b)}<http://ibt.lbl.gov>; Electronic mail: apersaud@lbl.gov

The detection of the alpha particle in a position-sensitive detector provides information about the direction and time the neutron was emitted. The high-energy neutron can exit the vacuum chamber and excite a nucleus in the assayed sample by inelastic scattering. The de-excitation, which for the nuclei of interest in the soil application occurs on a picosecond timescale, is accompanied by the emission of one or more gamma rays with energies characteristic of the isotope. These gamma rays can be detected with a fast scintillator and their times and energies recorded. Based on the time difference between the alpha and gamma detection together with the calculated associated neutron direction, the position of the inelastic scattering reaction can be calculated. By measuring many of these events, 3D elemental density profiles of the object of interest can be reconstructed. This process is exemplified in Figure 1, which shows a particular case where the inelastic scattering in a ^{12}C nucleus leads to the production of a prompt gamma ray.

The origins of API can be traced back to the '50s and '60s when the associated particle method (APM) was introduced with the main objective of reducing the induced gamma background (e.g. Okhuysen *et al.*⁹ and Csikai¹⁰) by recording gamma rays in coincidence with the associated particle in a DD or DT fusion reaction, i.e. ^3He or ^4He , respectively. In an early proof-of-principle paper Beyerle *et al.*¹¹ obtained 2D projections for different materials (water and table salt), hence showing some of the most important capabilities of this technique. Since then, API has found many uses in different areas of research and industry including detection of illicit drugs¹², explosives¹³, special nuclear material (SNM)¹⁴, diamond search¹⁵, and space exploration¹⁶, among many other applications. Fast scintillators, fast electronics, and high-resolution position-sensitive photomultiplier tubes have recently enabled both sub-nanosecond time resolution and sub-millimeter position resolution. This combination allows for the possibility of imaging objects with centimeter scale resolution.

II. SYSTEM OVERVIEW

The high-resolution system that we developed is intended for proof-of-principle demonstration. A commercial system for carbon in soil measurements would require more gamma detectors, the operation of the neutron generator at significantly higher output rates, and an alpha detector readout capable of handling rates on the order of 10^7 α/s . The arrangement of the neutron generator, gamma-ray detectors, and shielding for the measurements reported in this paper is shown in Figure 10a).

The neutron generator is a compact, sealed-type API tube (DT108API, Adelphi Technology¹⁷) with a microwave ion source driven by a solid-state power supply (Sairem GMS200WSM56) which couples to the plasma chamber via a square waveguide with a three-stub tuner. The titanium target, where neutrons are produced, is located inside the vacuum chamber (the generator head) centered underneath the Yttrium Aluminum Perovskite (YAP) scintillator (manufac-

tured by Crytur¹⁸) and a 6-inch sapphire window. This arrangement allows for the scintillation photons produced by the alpha particles striking the YAP crystal to be transported to the outside of the vacuum chamber where a position-sensitive photomultiplier tube (PSPMT, Hamamatsu H13700-03¹⁹) is used to detect the light signals. The gamma detectors, a LaBr_3 crystal (Saint-Gobain, 3-inch, B390S), and a NaI crystal (Alpha Spectra, 5-inch, 20I20/5(9823)BN), are positioned outside the tagged-neutron cone at the same height as the interrogated samples. Both detectors are shielded from the direct neutron flux by 12 inches of high-density polyethylene placed between the generator and the detectors. The detectors themselves are surrounded by lead bricks on four sides. The surface of the detectors facing the interrogated samples are only covered with a thin lead shield (2 mm). The surface facing away from the samples is not shielded and allows for signal and high voltage cable connections. Finally, the data acquisition is performed with a 16-channel fully digital system (XIA, PIXIE-16 Rev. F, 500 MHz ADC with 100 MHz FPGAs²⁰). Seven signals from the detectors are preamplified and fed into the PIXIE-16 for digitization and processing. Signals from the gamma detectors and that of the penultimate dynode of the alpha detector photomultiplier tube are time-stamped using a digital Constant Fraction Discrimination (CFD) algorithm. Additionally, signal amplitudes are determined for the gamma signals (energies) and the four corner signals of the alpha detector. If an alpha and a gamma signal fall within a set coincidence time window the event times and pulse height values are recorded.

III. POSITION-SENSITIVE ALPHA DETECTOR

The alpha detector allows to tag neutrons emitted into a cone, known as the API cone, and to determine the direction of the neutron and its time of flight. The design goal of a final position resolution of 5 cm at a distance of 60 cm from the source led to the following requirements for the alpha detector. The alpha-gamma time resolution needs to be better than 1 ns, because a 14.1 MeV neutron travels approximately 5 cm ns^{-1} . For the lateral dimensions, a 1 mm position resolution on the alpha detector is required due to geometry considerations regarding the size of the neutron producing beam spot and a distance of at least 60 cm between the neutron production site and the target nucleus. Since the YAP scintillator is located 6 cm from the neutron production site, it also experiences a high alpha rate. For our geometry, the expected alpha rate is 10^7 α/s for a generator output of 2×10^8 n/s . The design details of the alpha detector and its performance characterization are presented in Unzueta *et al.*²¹ and only summarized here. The scintillator signal needs to have a short rise time for optimal time resolution, a fast decay time for reduced pileup at the expected high count rate, and a sufficient light output for accurate position determination. The cerium-doped YAP inorganic scintillator was chosen due to the following reasons: it can withstand vacuum bakeout temperatures, it has a fast response (rise time of approximately 3 ns), a short decay time of 27 ns, a high light yield of approximately 5000 photons/MeV

for alpha particles (17000 to 20000 photons/MeV for gamma rays), and sufficient energy resolution (20% for 5 MeV alphas). It is also non-hygroscopic and hence easy to handle. The YAP scintillator is coupled to the PSPMT via a sapphire window vacuum interface. The finite-element software package COMSOL Multiphysics²² was used to optimize the geometry, understand the light spread onto the photocathode, estimate the total light transmission, and simulate the position reconstruction based on a 4-corner readout scheme. The main parameters chosen for the simulations are shown in Table I.

The surface of the YAP facing the incoming flux of alpha particles is coated with a reflective aluminum layer with a thickness of 400 nm to increase the number of photons that reach the photocathode per alpha interaction. This allows for improved photon statistics, and hence an improved position resolution. Figure 2 shows the COMSOL simulation results of one alpha interaction and its resulting light spread onto the photocathode with and without the reflective surface.

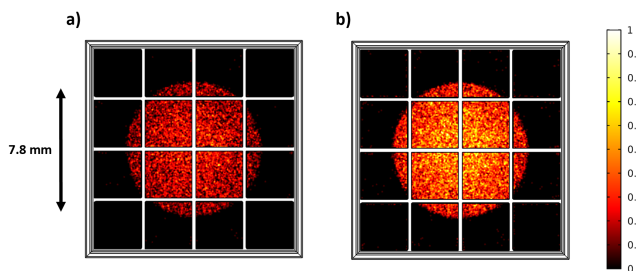


FIG. 2. COMSOL simulation of scintillation photon transport through one-sixteenth of the alpha detector system showing a) the transmitted light with no mirror surface, and b) the transmitted light with the mirror surface. The transmission increases by a factor of 2 to approximately 6.6% with no significant change in the diameter of the light projection onto the photocathode. The light spread directly influences the position reconstruction and readout. The white lines indicate the detector pixels.

The spread of the scintillation light over several pixels makes it possible to determine the center-of-gravity position with a sub-pixel resolution based on the following reconstruction algorithm

$$\begin{aligned} x &= \frac{A+B}{A+B+C+D} \\ y &= \frac{A+C}{A+B+C+D}, \end{aligned} \quad (2)$$

where A, B, C, and D are the energy values read at each corner of the 4-corner readout scheme. However simple, this algorithm also introduces positional errors particularly near the edges of the detector, which collect only a fraction of these photons. This effect was studied using the simulation software LTspice²⁴ and the results are shown in Figure 3. This edge effect can be corrected with more advanced reconstruction techniques aided by simulations, and the details will be further discussed in a future paper.

In order to experimentally quantify the position resolution and uniformity of the alpha detector, aluminum masks

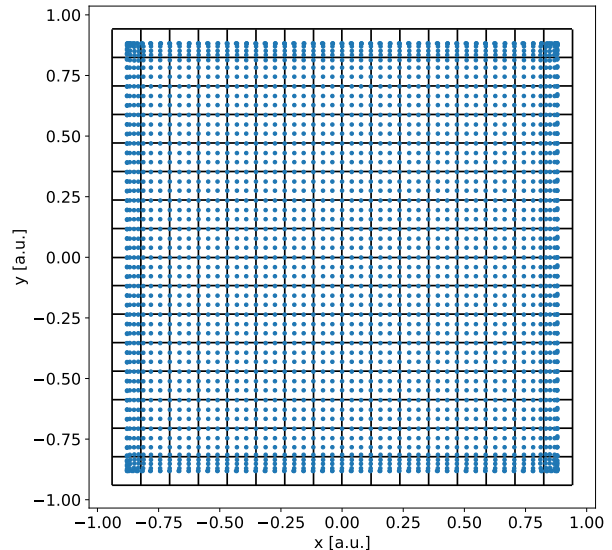


FIG. 3. LTspice output showing the resulting calculated position (blue dots) from a distributed DC current source. The source distribution derived from the COMSOL light collection simulations was applied every 0.9 mm and used to simulate the charge collection on neighboring anodes following an alpha particle hit. The reconstruction was done using Equation 2. The black-lined squares are the PMT pixels. Simulations show a high degree of uniformity except near the edges.

with different hole patterns were placed in between an ²⁴¹Am (3.9 MBq) alpha source and the YAP crystal in a separate 6-inch cube vacuum chamber. ²⁴¹Am decays primarily by the emission of an alpha particle with an average energy of approximately 5.5 MeV, which is higher than the alpha energy of 3.5 MeV from the DT reaction. Hence, the position reconstruction is expected to be the same, but the higher photon yield results in lower statistical variations.

Figure 4 (left) shows a mask with 256 apertures separated by 3 mm center-to-center, which is the same as the separation between individual pixels in the PSPMT. These two masks were placed close to the YAP crystal and 10 cm away from a ²⁴¹Am source. This system was placed inside a vacuum chamber evacuated to a few mTorr, and coincident data was taken for 200 s. The 6 inch flange with the sapphire window, YAP holder, and one of the masks are shown in Figure 5.

The position reconstruction was performed using Equation 2. The resulting image corresponding to the 256-hole mask is shown in Figure 6. Note the high spatial uniformity except near the edges where light spread is not uniform as predicted in the LTspice simulations above. Additionally, we observe a small non-linear effect (see curvature at the top and bottom) of each reconstructed image that we believe is due to stray capacitance on the readout board.

Additionally, notice how even though a 16×16 mask was used, only a 14×14 array is observed in Figure 6, as pre-

Name	Material	Thickness (mm)	Refractive Index (at 370 nm)
Photocathode	Bialkali	–	–
PMT window	UV glass	1.5	1.5354
Optical grease	PhenylSiO ₂ CH ₃	0.06	1.466
Vacuum interface	Sapphire	3.0	1.7925
Vacuum layer	Vacuum	0.005	1.0
YAP(Ce)	YAIO ₃	1.0	1.931
Mirror layer	Aluminum	0.0004	–

TABLE I. Main parameters used in COMSOL simulations. The thicknesses shown for the YAP and sapphire window are the ones chosen for the API system. Most values for the indices of refraction (n) were obtained from Refractive Index Database²³.

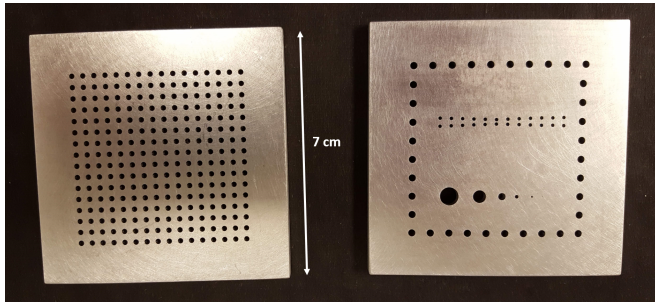


FIG. 4. Different aluminum mask designs used for the alpha detector performance tests. The flood-field mask on the left has 256 apertures with a 3 mm center-to-center separation, the same separation as for the PSPMT pixels. The mask on the right was designed to determine the position resolution of the alpha detector.

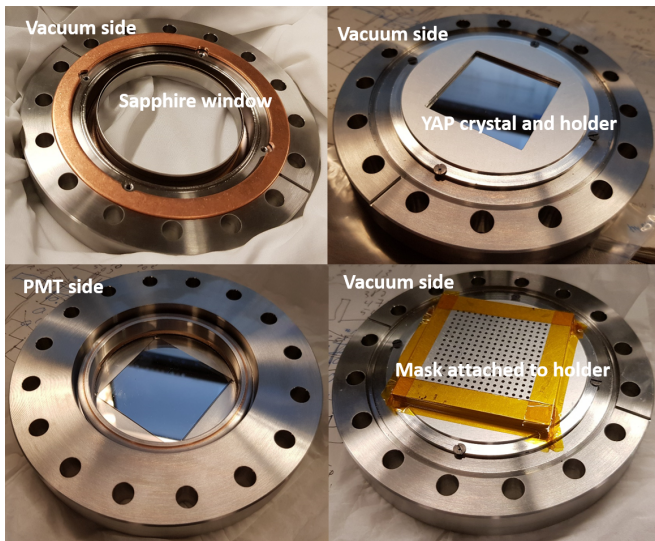


FIG. 5. Setup used to test the response of the YAP crystals, the uniformity of the reconstruction algorithm, and the achievable resolution. The sapphire window, YAP, and aluminum holder shown are the same as the ones mounted on the neutron generator.

dicted by COMSOL and LTspice simulations shown in Figure 3, which shows this non-linear edge effect.

Figure 7 shows the experimental results of using the mask on the right of Figure 4 with a hole pattern with decreasing

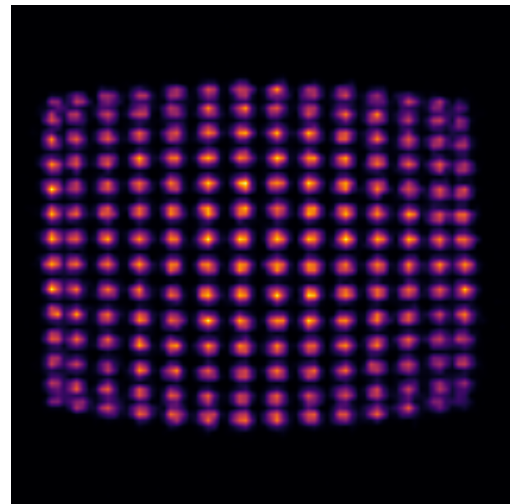


FIG. 6. Position reconstruction of the mask configuration shown on the left of Figure 4 using Equation 2.

center-to-center distance specially designed to measure the position resolution of the system. Notice that even apertures that are 0.2 mm apart (edge-to-edge) can be resolved with our current setup, which improves upon previous work such as Zhang *et al.*²⁵. This position resolution is five times better than the requirement of 1 mm stated in the introduction.

IV. PIXIE-16 DATA ACQUISITION SYSTEM

The PIXIE-16 is an all-digital waveform analyzer that operates at 500 MHz. Some of its capabilities regarding energy and time determination in the context of our application are described below.

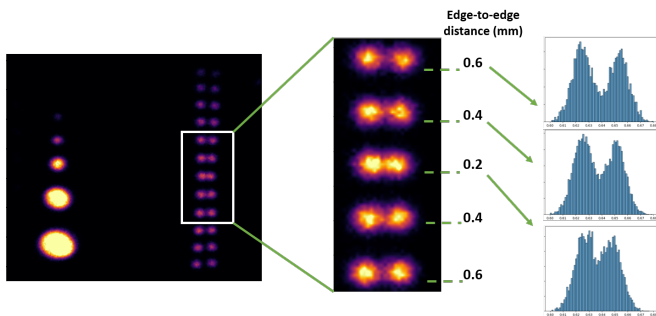


FIG. 7. Position resolution test of our detector system showing a series of holes separated by varying distances. Note that the minimum separation between the holes (edge-to-edge) is 0.2 mm and that these can be clearly resolved.

A. Energy determination

The PIXIE-16 implements a filter design that allows for some degree of pileup correction in the sense that it can correctly measure the energy of a pulse that is on top of another one having a single decay constant. The details of the algorithm can be found in Tan *et al.*²⁶ However, pileup correction was not used in the measurements reported here. We plan to implement the pileup correction for future experiments involving higher neutron rates. For the set of measurements presented in this article, the PIXIE-16 was set to integrate the full energy peak with the proper baseline subtraction. This approach works well for low event rates (alphas and gammas). For reference, using a standard ^{22}Na radioactive source we obtained an energy resolution of 3% at 511 keV for the LaBr₃ detector, which agrees well with the data provided by the manufacturer.

B. Time determination

The arrival times of the alpha particle and the gamma ray, which are used to calculate the neutron time of flight, need to be measured with excellent resolution for calculating the depth of interaction. As noted previously, achieving the goal of a depth resolution of 5 cm requires a time resolution of approximately 1 ns. The time resolution depends on the intrinsic properties of the detector and the signal processing electronics. For a more in-depth discussion regarding state-of-the-art timing techniques and differences between analog and digital systems, refer to publications such as Jokhovets *et al.*²⁷ A digital constant fraction discrimination algorithm (CFD) is implemented in the PIXIE-16 for determining the pulse arrival time. The advantage of the CFD method is a much smaller signal time walk obtained by determining the arrival time at a constant fraction of the pulse amplitude. The CFD algorithm implemented in this version of the PIXIE-16 is shown

in Equation 3.

$$CFD(k) = w \left(\sum_{i=k}^{k+L} a(i) - \sum_{i=k-B}^{k-B+L} a(i) \right) - \left(\sum_{i=k-D}^{k-D+L} a(i) - \sum_{i=k-D-B}^{k-D-B+L} a(i) \right), \quad (3)$$

This equation has four free parameters, w , B , D , and L . The constant fraction w varies between 0 and 1, and the other three are integer values indicating a number of points in the digitized trace. Finally, the ADC trace data is denoted by $a(i)$.

Due to the implementation details of the CFD algorithm in the FPGA, the parameters cannot be arbitrarily chosen. For example, the integration times are constrained to multiples of five because the clock frequency of the FPGAs (100 MHz) is five times lower than the digitizer frequency (500 MHz). The parameters were optimized offline for the three different detectors of the API system. We analyzed coincident signal traces collected with a ^{22}Na source that emits two 511 keV gamma rays simultaneously. The results indicated that the parameter that makes the most significant change is w , the multiplicative factor by which the trace amplitude is reduced to a certain fraction. The time resolution of the system improves as w decreases. However, at the same time the peak of the CFD trace that is used for triggering becomes smaller in amplitude, and hence the CFD threshold has to be set closer to the noise level, which sets a lower limit on w . The optimal value of w that could be implemented in custom firmware was 0.3125. As can be seen in Figure 8, a time resolution of 1.73 ns was achieved, which is an improvement of 300 ps compared to the standard firmware with a w value of 1. The

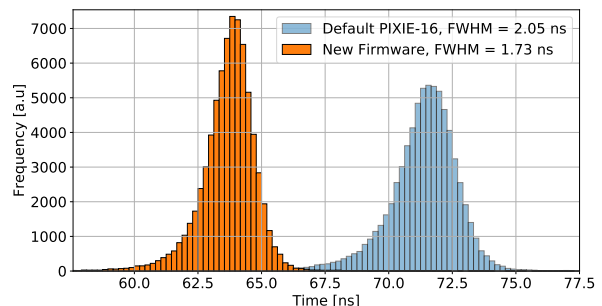


FIG. 8. CFD calculation for default PIXIE-16 parameters compared to the case where only w is changed from 1 to 0.3125 for the YAP-LaBr₃ combination. Note the time resolution improvement of approximately 300 ps. Note: the time resolution of the actual API system is significantly better due to the higher signal amplitudes generated by the alpha particles and higher energy gamma rays.

actual system has an even better time resolution with an upper limit of 1.25 ns (equivalent time calculated from the Z resolution discussed below also includes effects of scattering and reconstruction errors therefore the quoted time resolution is an upper limit) because INS gamma rays from carbon have higher energy compared to ^{22}Na and therefore better photon statistics resulting in less noisy rise times.

The appropriate time windows to be implemented in the data acquisition (DAQ) logic depend on the arrival times of the coincident alpha particle and gamma rays. The main components are the flight times of the neutron and alpha particles (geometry dependent), and the electron transit times of the respective photomultiplier tubes. Experimental data indicate a total time delay between the alpha (YAP) and gamma (LaBr₃) signals of approximately 80 ns. Events are being recorded in coincidence logic when two out of three detectors trigger within a time window of 30 ns. Therefore, in addition to alpha-gamma events, we also record gamma-gamma events. However, the latter do not appear at a significant rate due to the several order of magnitude lower gamma count rates and are then discarded during the offline data analysis. The resulting pre-processed data is recorded and used for further analysis.

V. API SYSTEM PERFORMANCE

The overall performance of API systems can be quantified in terms of its position resolution in 3D and its ability to obtain a prompt gamma-ray spectrum from a specific volume in a given time. The measurement time will vary depending on the nature and size of the interrogated sample, the number of gamma detectors employed for the measurement, the capability of the alpha detector, and the neutron rate. The measurement time will ultimately be limited by a maximum neutron rate of about 2×10^8 n/s where accidental coincidences between gamma and alphas will start dominating the signal²¹. In the following discussion, we focus on the resolution of the API system and the gamma response to specific samples relevant to soil composition.

A. API reconstruction algorithm

The pre-processed data from the DAQ are used to reconstruct the 3D location of a neutron-induced inelastic scattering event followed by the emission of a prompt gamma ray. The (x_0, y_0) position on the YAP crystal of the alpha detector is calculated from the 4-corner energies as explained in Section III. Figure 9 illustrates how the scattering location (x, y, z) in the sample is then calculated based on simple vector algebra. If we assume a neutron point source located at a known distance from the YAP crystal, we can calculate the direction of the velocity vector of the alpha particle, \vec{a} . Assuming that the neutron travels in the opposite direction of that alpha particle and together with the measured time between the alpha and gamma arrival, we can calculate the position of the scattering location by solving a quadratic equation that takes the time of flight of the gamma and neutron into account. The mathematical details of the algorithm can be found in Ref. 28.

The main assumptions in the reconstruction are that the neutrons are monoenergetic (14.1 MeV) and emitted from a point source, the neutron and associated alpha are emitted exactly 180° from each other in the lab system, and the position of the gamma detector is a point in space. Additionally, the

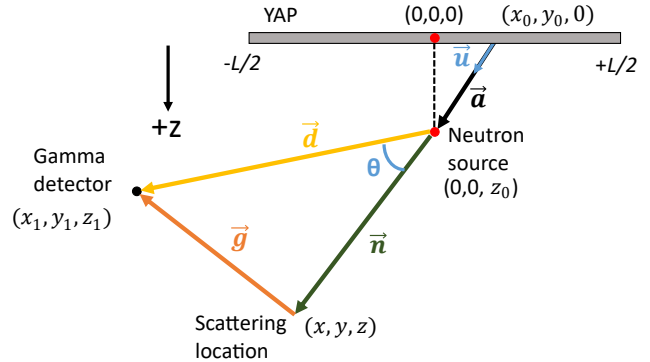


FIG. 9. Schematic representation (not to scale) of the API reconstruction technique based on vector algebra.

alpha, gamma, and neutron are taken to have fixed velocities for subsequent calculations. All of these assumptions are approximations of the actual system and each of them contributes to the overall error in the position reconstruction. In our design the main contribution to the angular uncertainty of the emitted neutrons is due to the size of the ion beam spot on the neutron generating target of approximately 2 mm and the position resolution of the alpha detector of < 0.5 mm. Other contributions are multiple scattering of the alpha particles in the target material and the dependence of the angle between the alpha and the neutron on the energy of the incoming deuteron (or triton) that decreases as it penetrates deeper into the target material before reacting with a triton (or deuteron). Both of these contributions are significantly smaller than the geometric uncertainty of about 2° for an X-Y resolution at 60 cm distance of about 2 cm. The depth resolution is dominated by the timing uncertainty given that a 14.1 MeV neutron travels approximately 5 cm per nanosecond. Instead of performing an error analysis based on detailed calculations, we experimentally measured the spatial resolution of the system as described below.

B. Position resolution

In order to test the system resolution in three dimensions, we performed a series of experiments using graphite bricks (99% ¹²C) and detecting the single INS gamma ray of 4.439 MeV. The experimental results presented below were obtained with the LaBr₃ gamma-ray detector, which has better time and energy resolution than the NaI detector. The graphite samples were arranged in two different configurations: 1) two thin (1 cm) slabs stacked in Z with varying distances between them in order to measure the depth resolution, as shown in Figure 10b) and 2) two thick (6 cm) graphite bricks placed next to each other (X-Y plane) and their distance varied along the X dimension, as shown in Figure 10c). The neutron generator was operated at 50 kV producing a neutron output of $\approx 5 \times 10^6$ neutrons/s.

Figure 11 shows the experimental results for three different

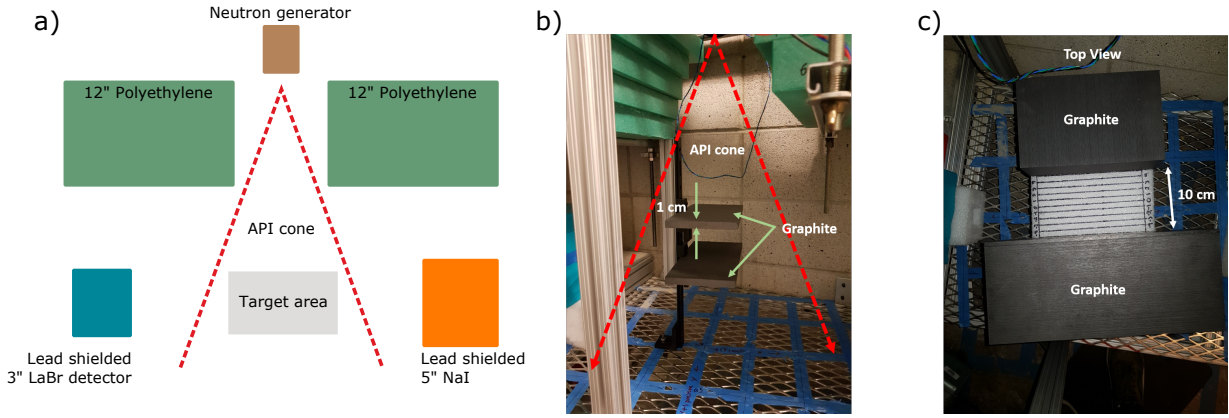


FIG. 10. Experimental setup used to characterize the system: a) schematic of the setup showing the position of the neutron source, the shielding and the detectors b) depth resolution measurement using thin (1 cm) graphite slabs, and c) X-Y resolution using thick (6 cm) graphite bricks.

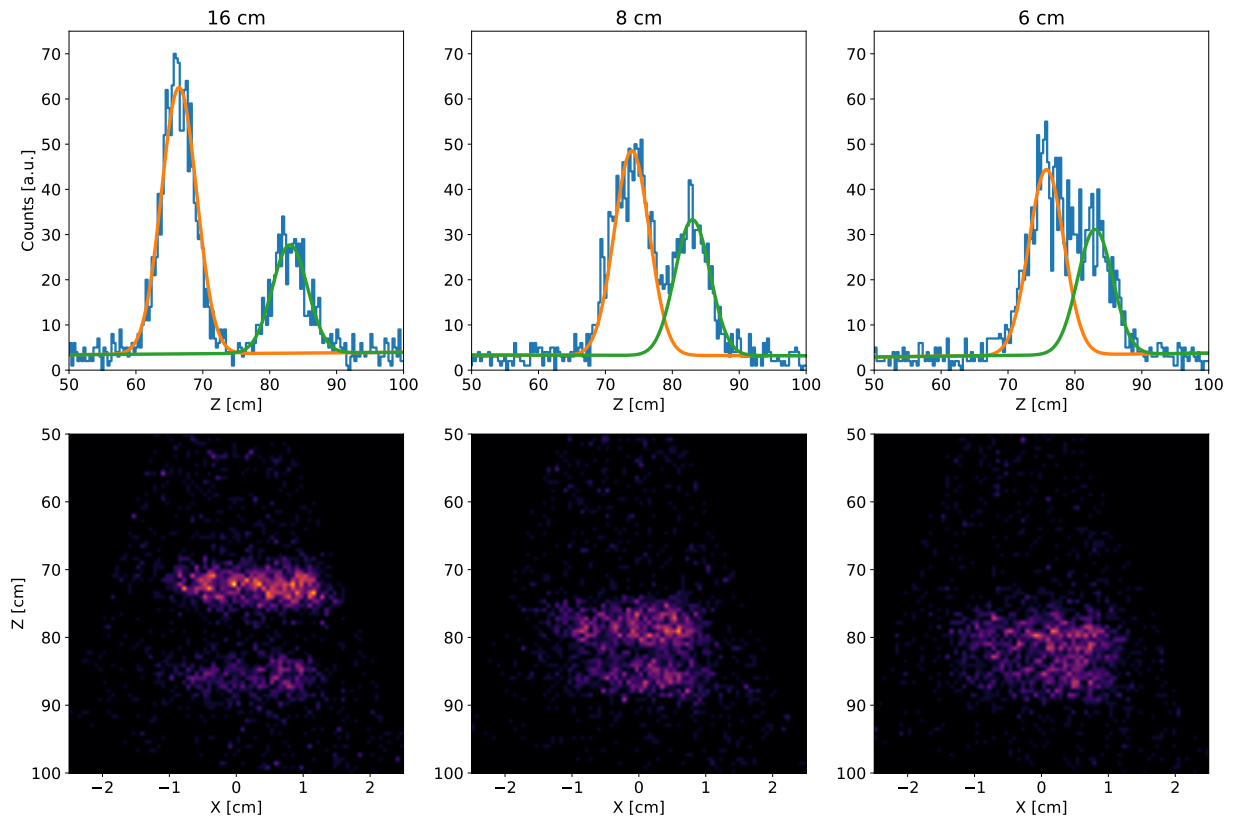


FIG. 11. LaBr_3 experimental results for the depth resolution measurements with two thin graphite slabs with varying distances among them. The bottom plots show X-Z intensity maps of the 3D locations of the reconstructed events and the top plots show the integrated counts vs. Z with Gaussian curves used to fit the two peaks. Note that at 16 cm separation, the two slabs are clearly separated. The intensity maps also show the top slab being exposed to a higher neutron flux as expected.

cases where the top graphite slab was brought closer to the bottom one starting at 16 cm separation between them. The irradiation time for each case scenario was one hour. The data was processed by selecting events of 4.439 MeV gamma energy together with its single escape peak and by selecting only the graphite area in the X-Y plane. The intrinsic depth resolution of the system is shown in Figure 11 where the two

slabs are resolved down to a distance of about 6 cm. The measured Z-resolution, defined by the full width half maximum (FWHM) of the Gaussian fit, for the LaBr_3 -YAP combination is 6.2 ± 0.1 cm.

The system X-Y resolution was measured similarly with the arrangement shown in Figure 10c) where two thick graphite bricks were placed side by side separated initially by 10 cm.

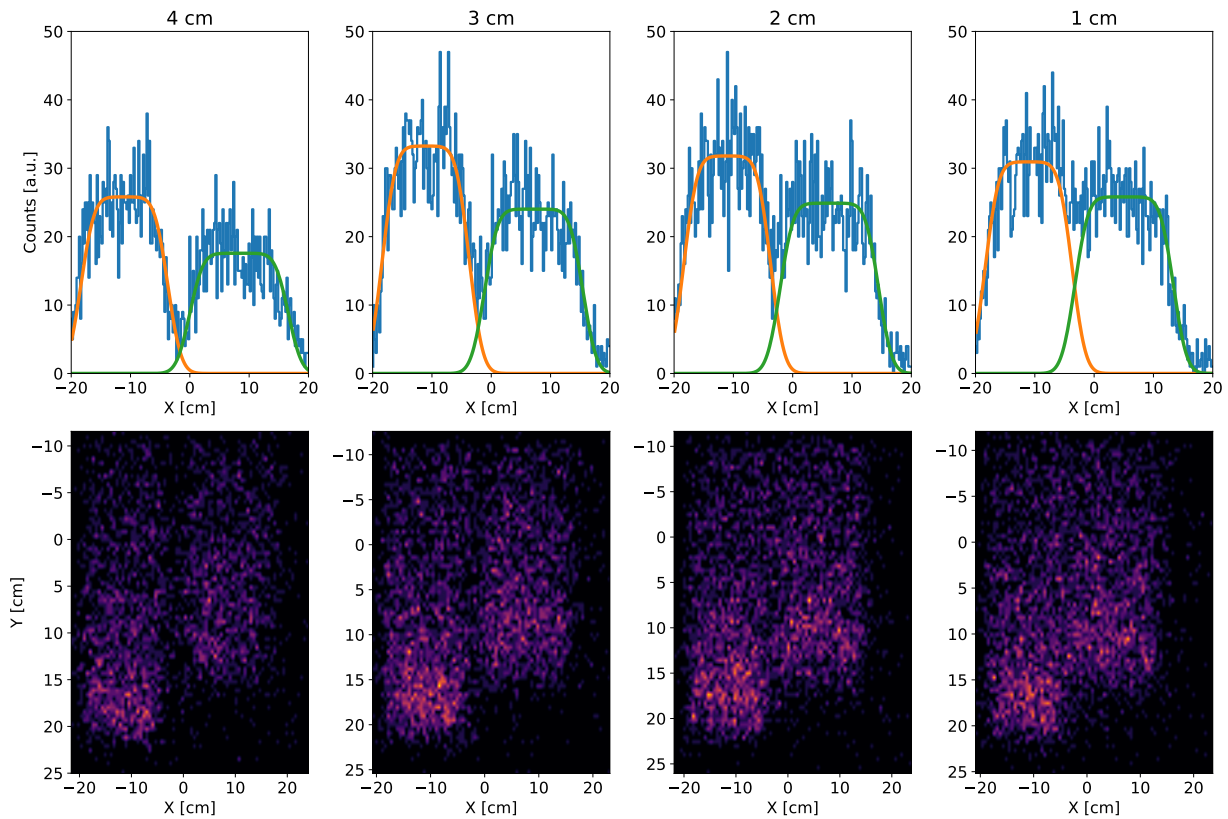


FIG. 12. LaBr_3 experimental results for the system X-Y resolution measured with graphite bricks. The bottom plots show X-Y intensity maps of the 3D locations of the reconstructed events and the top plots show the integrated counts vs. X with the sum of 200 Gaussian curves used to fit the two peaks.

The blocks were then brought together in one-centimeter steps. The irradiation time for each case scenario was 3000 s. 1D-Histograms of the measured data were globally fitted with the sum of 200 Gaussians equally spaced across a certain width. However, outwards scattering of neutrons near the edge of a graphite brick adds an additional fall off for the edges in the histogram and therefore the measured FWHM can only be used as an upper limit for the resolution of the instrument. Figure 12 shows the results of a representative set of these measurements where a FWHM of 4.2 ± 0.2 cm was measured. Looking at Figure 12 one would assume that the resolution is about 1 to 2 cm (where the FWHM points touch), but due to the additional falloff at the edges this is only a lower limit. The real instrument resolution therefore is between 2 to 4 cm.

Even though these measurements were performed along the direction transverse to the detector (X-axis), reconstructed images (not shown) indicate the same resolution in the direction of the detector (Y-axis) as expected from the symmetry of the alpha detector.

C. Single-element gamma response

As mentioned previously, one of the most important characteristics of the API technique is the ability to obtain prompt

gamma spectra from a specific volume, so that background gammas from surrounding materials or delayed emission (such as from neutron capture) are greatly reduced. Therefore, we measured single-element spectra of the main elements in soil in order to generate energy spectrum templates for future soil analysis and to validate MCNP6 simulations. Figure 13

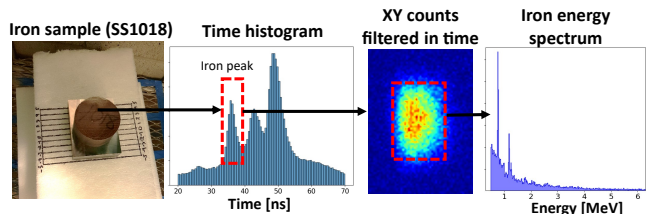


FIG. 13. Example of the analysis procedure for obtaining elemental gamma spectra for specific elements. The photograph of the sample is a top view from the perspective of the neutron generator. The LaBr_3 detector is located to the left of it.

shows an iron sample (SS1018) of 3.16 kg that was irradiated for 100 min using a neutron generator voltage of 50 kV. The sample was placed approximately 60 cm underneath the neutron generator. From the measured data X, Y, and Z coordinates are calculated and the events are restricted to the volume of the sample under test. An energy histogram of all the events

inside this volume is then generated. The inelastic gamma spectrum of natural iron as measured is shown on the right of Figure 13.

The same procedure was used to obtain element-specific gamma spectra for various elements identified as the most abundant in forest and agricultural soils: carbon, aluminum, oxygen, iron, and silicon.

The measured spectra were generally linear up to the carbon peak but showed some non-linearity at higher gamma-ray energies. Therefore, we used a linear + quadratic calibration function. The measured elemental energy spectra served to benchmark our MCNP6 simulations. Simulations are generally needed in order to design the instrument, plan future experiments, and understand the sensitivity of the system to different elemental concentrations. They can be used to optimize specific design parameters and can support the analysis of experimental data. We simulated the experiment in two steps: 1) Neutron-induced gamma-ray production in the sample and 2) gamma-ray transport to the detector with its specific response function. Figure 14 shows the measured spectra

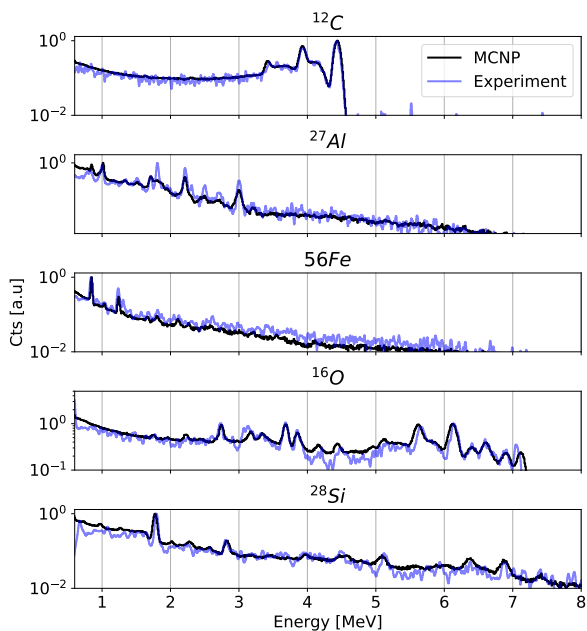


FIG. 14. Comparison between measured gamma-ray spectra and MCNP6 simulations for elements relevant to soil composition. Note the overall agreement. However, there are significant discrepancies for ^{27}Al , in particular. The spectra were normalized by the highest peak.

with their corresponding simulation. While there is generally good agreement, there are some significant discrepancies in relative intensities such as for the 1.72 MeV gamma-ray line from $^{27}\text{Al}(n,n'\gamma)$ originating from the transition $2.73\text{ MeV} \rightarrow 1.01\text{ MeV}$. The ENDF /B-VI library was used because of its better agreement with experiments compared to most current releases of ENDF²⁹. The reason seems to be the attempt to

transition from natural compounds to individual isotopes in later versions, which created gaps and overall poorer agreement with experimental data³⁰. The results presented in Figure 14 show the capability of the system to analyze samples within a small volume and obtain their gamma signature. It is possible to create a library of response functions for specific elements, and by matching samples with a more complex composition determine their relative abundance (basic component analysis). This approach is sometimes used in the oil exploration industry³¹. However, for large soil samples, simple template matching will not be enough since the energy distribution of neutrons at depth will not be monoenergetic anymore due to scattering in the top layers of the soil, and therefore the elemental response will be different from that of the measured spectra shown in Figure 14.

VI. RESULTS AND CONCLUSIONS

A prototype of an all-digital high-resolution associated particle imaging system for the determination of isotopic 3D distributions in soils has been built. We found that our approach of coupling a monolithic YAP crystal to a sapphire vacuum window gave superior resolution and higher light yields than previously developed approaches using fiber-optic faceplates, such as in Cates, Hayward, and Zhang³². Experimental tests showed that the position of the alpha particle can be measured with a resolution of 0.2 mm using a four-corner readout scheme.

The API system was characterized in terms of its position resolution and its ability to identify specific isotopes relevant to soil chemistry. We demonstrated a system lateral (X-Y) resolution between 2 to 4 cm and a depth (Z) resolution of $6.2 \pm 0.1\text{ cm}$ using a graphite sample. The depth resolution is mainly dependent on the time resolution and we achieved noticeable improvements by implementing a custom firmware that optimizes the CFD parameters. Further optimizing the CFD parameters or switching to a different algorithm to measure the arrival time of the particles³³ could lead to even better depth resolution.

We obtained gamma-ray spectra from different elemental materials including ^{12}C , ^{16}O , ^{28}Si , ^{27}Al , and ^{56}Fe and used these data to benchmark Monte Carlo simulations. We found generally good agreement confirming that the radiation transport code MCNP6 can be used to optimize the system and support the data analysis.

Currently, the maximum neutron rate the system can operate at is limited by pileup on the alpha detector due to the long RC delays introduced by the four-corner resistive network used to read out the position of the alpha particle. Data presented in this paper was taken at a neutron rate of 5×10^6 neutrons/s. However, the system also works with minimal position degradation at rates up to 1×10^7 neutrons/s (not shown). Utilizing the built-in pileup correction of the PIXIE-16 will increase the rate capability further. However, in order to achieve the full rate capability of an API system of 2×10^8 neutrons/s, faster readout designs, such as reading out rows and columns instead of just the four corners, are under

development.

In conclusion, the results presented indicate that this API system will meet the design goals for measuring the carbon distribution in soil once higher rate capabilities are implemented. We also demonstrated that the system can be used to measure energy spectra for $5 \times 5 \times 5 \text{ cm}^3$ voxels over a $50 \times 50 \times 30 \text{ cm}^3$ sample volume. Measured responses from single elements agree with MCNP6 simulations. Work in progress includes switching to an improved setup²⁸ allowing operation at higher neutron rates. Additionally, we need to characterize neutron scattering effects and attenuation in soil. Finally, we also need to implement models to reconstruct soil elemental densities.

AUTHOR'S CONTRIBUTION

All authors contributed to writing and editing the paper and to the experimental work. Mauricio Ayllon Unzueta did most of the measurements discussed in this paper and ran all MCNP6 simulations. Tanay Tak worked mostly on the SPICE simulations and the X-Y reconstruction in the alpha detector. Mauricio Ayllon Unzueta, Bernhard Ludewigt, and Arun Persaud worked on the instrument design, experimental setup, data acquisition system, and data analysis. Arun Persaud worked on the hardware control and is also the principal investigator of the project.

DATA AVAILABILITY

The data, analysis scripts, and simulation scripts are openly available on Zenodo at <https://doi.org/10.5281/zenodo.4008740>, reference number 34.

ACKNOWLEDGMENTS

The authors would like to thank Takeshi Katayanagi for his technical support. The information, data, or work presented herein was funded by the Advanced Research Projects Agency-Energy (ARPA-E), U.S. Department of Energy, under Contract No. DEAC02-05CH11231.

¹J. Sanderman, T. Hengl, and G. J. Fiske, "Soil carbon debt of 12,000 years of human land use," *Proc. Natl. Acad. Sci. U. S. A.* **114**, 9575–9580 (2017).

²J. Huang, B. Minasny, A. B. McBratney, J. Padarian, and J. Triantafyllis, "The location- and scale- specific correlation between temperature and soil carbon sequestration across the globe," *Sci. Total Environ.* **615**, 540–548 (2018).

³D.-S. Veres, "A comparative study between loss on ignition and total carbon analysis on late glacial sediments from atteköps mosse, southwestern sweden, and their tentative correlation with the grip event stratigraphy," (2001), student Paper.

⁴ARPA-e ROOTS program, <https://arpa-e.energy.gov/?q=arpa-e-programs/roots> (2018).

⁵L. Wielopolski, I. Orion, G. Hendrey, and H. Roger, "Soil carbon measurements using inelastic neutron scattering," *IEEE Transactions on Nuclear Science* **47**, 914–917 (2000).

⁶L. Wielopolski, G. Hendrey, K. H. Johnsen, S. Mitra, S. A. Prior, H. H. Rogers, and H. A. Torbert, "Nondestructive system for analyzing carbon in the soil," *Soil Sci. Soc. Am. J.* **72**, 1269–1277 (2008).

⁷A. Kavetskiy, G. Yakubova, S. A. Prior, and H. A. Torbert, "Application of associated particle neutron techniques for soil carbon analysis," *AIP Conf. Proc.* **2160**, 050006 (2019).

⁸A. Kavetskiy, G. Yakubova, S. A. Prior, and H. A. Torbert (USDA), "Application of Neutron-Gamma technologies in agriculture," *TRANS* **121**, 539–541 (2019).

⁹P. L. Okhuysen, E. W. Bennett, J. B. Ashe, and W. E. Millett, "Detection of fast neutrons by the associated particle method," *Review of Scientific Instruments* **29**, 982–985 (1958), <https://doi.org/10.1063/1.1716073>.

¹⁰J. Csikai, *CRC Handbook of Fast Neutron Generators* (CRC, Boca Raton, FL, 1987).

¹¹A. Beyerle, R. Durkee, G. Headley, J. P. Hurley, and L. Tunnell, "Associated particle imaging," in *Conference Record of the 1991 IEEE Nuclear Science Symposium and Medical Imaging Conference* (1991) pp. 1298–1304 vol.2.

¹²C. L. Fontana, A. Carnera, M. Lunardon, F. Pino, C. Sada, F. Soramel, L. Stevanato, G. Nebbia, C. Carasco, B. Perot, A. Sartet, G. Sannic, A. Iovene, C. Tintori, K. Grodzicki, M. Moszyński, P. Sibczyński, L. Swiderski, and S. Moretto, "Detection system of the first rapidly relocatable tagged neutron inspection system (rtnis), developed in the framework of the european h2020 c-bord project," *Physics Procedia* **90**, 279 – 284 (2017), conference on the Application of Accelerators in Research and Industry, CAARI 2016, 30 October – 4 November 2016, Ft. Worth, TX, USA.

¹³C. Carasco, B. Perot, S. Bernard, A. Mariani, J.-L. Szabo, G. Sannic, T. Roll, V. Valkovic, D. Sudac, G. Vjesti, M. Lunardon, C. Bottosso, D. Fabris, G. Nebbia, S. Pesente, S. Moretto, A. Zenoni, A. Donzella, M. Moszynski, M. Gierlik, T. Batsch, D. Wolski, W. Klamra, P. L. Tourneur, M. Lhuissier, A. Colonna, C. Tintori, P. Peerani, V. Sequeira, and M. Salvato, "In-field tests of the euritrack tagged neutron inspection system," *Nucl. Instrum. Methods Phys. Res. A* **588**, 397 – 405 (2008).

¹⁴Q. Ji, B. Ludewigt, J. Wallig, W. Waldron, and J. Tinsley, "Development of a time-tagged neutron source for snm detection," *Physics Procedia* **66**, 105 – 110 (2015), the 23rd International Conference on the Application of Accelerators in Research and Industry - CAARI 2014.

¹⁵V. Y. Alexakhin, V. M. Bystritsky, N. I. Zamyatin, E. V. Zubarev, A. V. Krasnoperov, V. L. Rapatsky, Y. N. Rogov, A. B. Sadovsky, A. V. Salamatin, R. A. Salmin, M. G. Sapozhnikov, V. M. Slepnev, S. V. Khabarov, E. A. Razinkov, O. G. Tarasov, and G. M. Nikitin, "Detection of diamonds in kimberlite by the tagged neutron method," *Nucl. Instrum. Methods Phys. Res. A* **785**, 9–13 (2015).

¹⁶M. Litvak, Y. Barmakov, S. Belichenko, R. Bestaev, E. Bogolubov, A. Gavrychenkov, A. Kozyrev, I. Mitrofanov, A. Nosov, A. Sanin, V. Shvetsov, D. Yurkov, and V. Zverev, "Associated particle imaging instrumentation for future planetary surface missions," *Nucl. Instrum. Methods Phys. Res. A* **922**, 19 – 27 (2019).

¹⁷Adelphi Technology Inc., <http://adelphitech.com/> (2018).

¹⁸CRYTUR, spol. s r.o., <https://crytur.cz> (2018).

¹⁹Hamamatsu Photonics K.K., <https://www.hamamatsu.com/us/en/product/type/H13700/index.html> (2018).

²⁰XIA LLC, <https://xia.com> (2018).

²¹M. A. Unzueta, W. Mixter, Z. Croft, J. Joseph, B. Ludewigt, and A. Persaud, "Position sensitive alpha detector for an associated particle imaging system," *AIP Conference Proceedings* **2160**, 050005 (2019), arXiv:1811.08591.

²²COMSOL Multiphysics v. 5.2, <https://www.comsol.com> (2018).

²³Refractive Index Database, <https://refractiveindex.info> (2019).

²⁴LTspice from Analog Devices, <https://www.analog.com/LTspice> (2018).

²⁵X. Zhang, J. P. Hayward, J. W. Cates, P. A. Hausladen, M. A. Laubach, J. E. Sparger, and S. B. Donald, "Benchmarking the geant4 full system simulation of an associated alpha-particle detector for use in a d-t neutron generator," *Applied Radiation and Isotopes* **70**, 1485 – 1493 (2012).

²⁶H. Tan, D. Breus, W. Hennig, K. Sabourov, W. K. Warburton, W. B. Doriese, J. N. Ullom, M. K. Bacrania, A. S. Hoover, and M. W. Rabin, "High rate pulse processing algorithms for microcalorimeters," in *2008 IEEE Nuclear Science Symposium Conference Record* (2008) pp. 1130–1133.

- ²⁷L. Jokhovets, A. Erven, C. Grewing, M. Herzkamp, P. Kulesa, H. Ohm, K. Pysz, J. Ritman, V. Serdyuk, M. Streun, S. V. Waasen, and P. Wintz, “Improved rise approximation method for pulse arrival timing,” *IEEE Transactions on Nuclear Science* **66**, 1942–1951 (2019).
- ²⁸M. A. Unzueta, *An Associated Particle Imaging System for the Determination of 3D Isotopic Distributions*, Ph.D. thesis, UC Berkeley (2020).
- ²⁹D. B. et. al., “Endf/b-viii.0: The 8th major release of the nuclear reaction data library with cielo-project cross sections, new standards and thermal scattering data,” *Nuclear Data Sheets* **148**, 1 – 142 (2018), special Issue on Nuclear Reaction Data.
- ³⁰Mauborgne, Marie-Laure, Allioli, Françoise, Manclossi, Mauro, Nicoletti, Luisa, Stoller, Chris, and Evans, Mike, “Designing tools for oil exploration using nuclear modeling,” *EPJ Web Conf.* **146**, 09036 (2017).
- ³¹R. J. Radtke, M. Lorente, B. Adolph, M. Berheide, S. H. Fricke, J. Grau, S. L. Herron, J. P. Horkowitz, B. Jorion, D. P. Madio, D. H. May, J. Miles, L. Perkins, O. Philip, B. Roscoe, D. A. Rose, and C. Stoller, “A new capture and inelastic spectroscopy tool takes geochemical logging to the next level,” (2012).
- ³²J. W. Cates, J. P. Hayward, and X. Zhang, “Achievable position resolution of an alpha detector with continuous spatial response for use in associated particle imaging,” in *2013 IEEE Nuclear Science Symposium and Medical Imaging Conference (2013 NSS/MIC)* (2013) pp. 1–3.
- ³³W. K. Warburton and W. Hennig, “New algorithms for improved digital pulse arrival timing with Sub-GSps ADCs,” *IEEE Trans. Nucl. Sci.* **64**, 2938–2950 (2017).
- ³⁴M. A. Unzueta, T. Tak, B. Ludewigt, and A. Persaud, “Data, analysis scripts, and simulations files for ‘achieving centimeter resolution with an all-digital associated particle imaging system for the 3d determination of isotopic distributions’,” 10.5281/zenodo.4008740 (2020), Zenodo.